Ion charge states and potential geoeffectiveness: the role of coronal spectroscopy for space-weather forecasting

Article

Published Version

Owens, M. J. ORCID: https://orcid.org/0000-0003-2061-2453, Lockwood, M. ORCID: https://orcid.org/0000-0002-7397-2172 and Barnard, L. A. ORCID: https://orcid.org/0000-0001-9876-4612 (2018) Ion charge states and potential geoeffectiveness: the role of coronal spectroscopy for space-weather forecasting. Space Weather, 16 (6). pp. 694-703. ISSN 1542-7390 doi: 10.1029/2018SW001855 Available at https://centaur.reading.ac.uk/77449/

Space Weather

RESEARCH ARTICLE
10.1029/2018SW001855

Ion Charge States and Potential Geoeffectiveness: The Role of Coronal Spectroscopy for Space-Weather Forecasting

M. J. Owens[1], M. Lockwood[1], and L. A. Barnard[1]

[1]Space and Atmospheric Electricity Group, Department of Meteorology, University of Reading, Reading, UK

Key Points:
- Ion charge states within interplanetary coronal mass ejections correlate with geoeffectiveness
- Coronal mass ejections formed in hot coronal regions are statistically more geoeffective than those formed in cooler coronal regions
- Coronal spectroscopy could provide advanced warning of geoeffective solar wind conditions

Correspondence to:
M. J. Owens,
m.j.owens@reading.ac.uk

Citation:
Owens, M. J., Lockwood, M., & Barnard, L. A. (2018). Ion charge states and potential geoeffectiveness: The role of coronal spectroscopy for space-weather forecasting. *Space Weather*, *16*, 694–703. https://doi.org/10.1029/2018SW001855

Received 1 MAR 2018
Accepted 23 MAY 2018
Accepted article online 31 MAY 2018
Published online 15 JUN 2018

Abstract Severe space weather is driven by interplanetary coronal mass ejections (ICMEs), episodic eruptions of solar plasma, and magnetic flux that travel out through the heliosphere and can perturb the Earth's magnetosphere and ionosphere. In order for space-weather forecasts to allow effective mitigating action, forecasts must be made as early as possible, necessitating identification of potentially "geoeffective" ICMEs close to the Sun. This presents two challenges. First, geoeffectiveness is primarily determined by the magnetic field intensity and orientation, both of which are difficult to measure close to the Sun. Second, the magnetic field evolves in transit between the Sun and the Earth, sometimes in a highly nonlinear way. Conversely, solar wind ion charge states, such as the ratio of O^{7+} to O^{6+}, are fixed by the electron temperature at the coronal height where ion-electron collisions are last possible as the ICME erupts. After this point, they are said to be "frozen in" as they do not evolve further as the ICME propagates through the solar wind. In this study we show that ion charge states, while not geoeffective in and of themselves, act as strong markers for the geoeffectiveness of the ICME. The probability of severe space weather is around 7 times higher in "hot" ICMEs than "cold" ICMEs, as defined by O^{7+}/O^{6+}. We suggest that coronal spectroscopy of ICMEs could complement current forecasting techniques, providing valuable additional information about potential geoeffectiveness.

1. Introduction

Predicting near-Earth solar wind conditions more than one day ahead is a major goal of space-weather forecasting. Simple statistical approaches can make great strides, particularly toward forecasting the quasi-steady component of the solar wind (Owens et al., 2013; Riley et al., 2017). But the most severe space-weather conditions are the result of interplanetary coronal mass ejections (ICMEs), episodic eruptions of solar plasma, and magnetic flux (Kilpua et al., 2017; Schwenn, 2006). The inherently transient nature of ICMEs means that dynamical forecasting techniques are required, and for subsequent mitigation strategies to be effective, these forecasts must be made as early as possible. As the typical ICME Sun-Earth transit time is around two to five days (Gopalswamy et al., 2001), advanced forecasting requires identifying potentially geoeffective ICMEs close to the Sun. ICME kinematics, an important component of the geoeffectiveness of CMEs, can be estimated in the corona and inner heliosphere from white-light observations provided by coronagraphs and heliospheric imagers (e.g., Davis et al., 2009, Yashiro et al., 2004). These estimates, however, are subject to complications associated with viewing angles and line-of-sight integration of scattered light, as well as assumptions about the CME geometry (Barnard et al., 2017). Nevertheless, these properties potentially allow an estimate of the arrival time of ICMEs in near-Earth space (Tucker-Hood et al., 2015). But the impact on the Earth system, the geoeffectiveness, is primarily determined by the strength and direction of the magnetic field within the ICME, which is extremely difficult to measure remotely (DeForest et al., 2017). (This is usually determined from in situ measurements by spacecraft in a halo orbit around the L1-Lagrange point as the ICME passes over them—by which time warnings are usually less than 30 min in advance.) Even if the remote observational challenges are overcome, there remains the issue of projecting near-Sun estimates to near-Earth predictions, as in-transit effects can greatly influence the properties of ICMEs at 1 AU (e.g., Gopalswamy et al., 2001; Manchester et al., 2017; Savani et al., 2010, and references therein).

Ion charge states in the solar wind are set by the coronal electron temperature at a few solar radii and are subsequently "frozen in" for the remainder of the flow (Feldman et al., 2005; Geiss et al., 1995; Gloeckler et al., 2003). Thus, coronal temperature, and hence ion charge states, is an observable coronal parameter for which in-transit solar wind effects are negligible. Of course, ion charge states are of little direct interest for space-weather forecasting. However, they can act as useful markers of different solar wind and ICME types (Henke et al., 1998; Lepri et al., 2001; Lepri & Zurbuchen, 2004), which may in turn reveal an indirect

relationship between coronal temperature and geoeffectiveness. This study introduces that relation first for the solar wind as a whole, then looks in more details for ICMEs.

2. Data

The geoeffectiveness of solar wind structures is a combination of both their intrinsic physical properties in near-Earth space and current state of the magnetosphere, including the relative orientation of the Earth's magnetosphere to the heliographic system, which varies systematically as a function of time of day and year (Rosenberg & Coleman, 1969; Russell & McPherron, 1973; Siscoe & Crooker, 1996). While the latter geometric effects are important for space weather (Lockwood et al., 2016), they are entirely deterministic and thus, in principle, can be readily incorporated into any space-weather forecasting scheme if the arrival time of the ICME at the magnetosphere is forecast accurately. Here these effects are removed from the analysis by exclusively considering in situ spacecraft data in heliographic radial-tangential-normal coordinates. This allows determination of the potential geoeffectiveness (G) of solar wind structures resulting solely from their intrinsic near-Earth properties. G is here defined as the potential of the solar wind to energize and perturb the magnetospheric system, for a fixed configuration of that system. A number of solar wind-magnetosphere "coupling functions" have been proposed, which essentially parameterize the dayside magnetospheric reconnection rate in terms of upstream solar wind conditions. We here use the Vasyliunas et al. (1982) formulation, which is derived from physics-based arguments, and quantifies the net energy input from the solar wind to the magnetosphere available to drive geomagnetic activity on a range of timescales. The terrestrial space-weather indices that respond most directly and simply to energy input to the magnetosphere are those which monitor the substorm cycle, in which extracted energy is stored in the geomagnetic tail during the growth phase and subsequently deposited in the inner magnetosphere and ionosphere in the expansion. Thus, these indices include the auroral electrojet indices, AU, AL, and AE, and convection indices such as transpolar voltage and the polar cap index, but also midlatitude "range" indices *am*, *aa*, and *ap* (Lockwood, 2013). Other indices, such as Dst or total ring current particle content are related but complicated by other factors and longer timescales (Lockwood et al., 2016). As we are interested only in the relative variation of G, constants are excluded to give

$$G = n_P^{(2/3-\propto)} B^{(2\propto)} v^{(7/3-\propto)} \sin^4(\theta/2) \quad (1)$$

where n_P is the solar wind proton number density, B is the heliospheric magnetic field (HMF; Owens & Forsyth, 2013) intensity, v is the solar wind speed, θ is the nonradial clock angle of the HMF (i.e., $\theta = \tan^{-1} B_T/B_N$, where B_T and B_N are the tangential and normal components of the HMF, respectively), and $\propto$ is the coupling exponent, empirically determined to be approximately 0.5 (Lockwood et al., 2017). For simplicity, we assume that the alpha-to-proton ratio is constant. Again, as only relative variations are of interest, units are arbitrary and values reported in this study are obtained from n_P in cm^{-3}, B in nT, and v in km/s.

Using $\propto = 0.5$, G varies most strongly with B, followed by v, with only a weak dependence on n_P (thus, the assumption of a constant alpha-to-proton ratio made in equation (1) is relatively unimportant). Most importantly, the $\sin^4(\theta/2)$ term acts as a half-wave rectifier, with G being rapidly reduced to zero when the normal component of the HMF (B_N) is northward. Thus, to first order, G approximates the heliographic dawn-to-dusk electric field, E_Y, long used as a proxy for geomagnetic activity (Dungey, 1961).

The base data for G used in this study are 5-min averages of ACE solar wind magnetic field and plasma data (McComas et al., 1998; Smith et al., 1998). Data were obtained from ftp://cdaweb.gsfc.nasa.gov and transformed to radial-tangential-normal coordinates. The 5-min time resolution is used as a proxy for rapid fluctuations, which can have space-weather implications, particularly on the power systems (e.g., Kappenman, 2003). One-day averages are also considered. While ICME properties, particularly the magnetic field orientation, are expected to vary significantly over such timescales, the largest geomagnetic storms are driven by persistent solar wind energy input (Gonzalez et al., 1999), and thus, one-day averages are a useful timescale to consider.

Solar wind composition and ion charge state information are provided by the ACE Solar Wind Ion Composition Spectrometer (SWICS) instrument (Gloeckler et al., 1998), here taken from the 3-hr "merged" data set at ftp://cdaweb.gsfc.nasa.gov/pub/data/ace/multi. We only show the oxygen charge state ratio, O^{7+}/O^{6+}, but we obtain qualitatively similar results using the carbon charge state ratio, C^{6+}/C^{5+}, or average O, C, or Fe charge states as markers of coronal temperature.

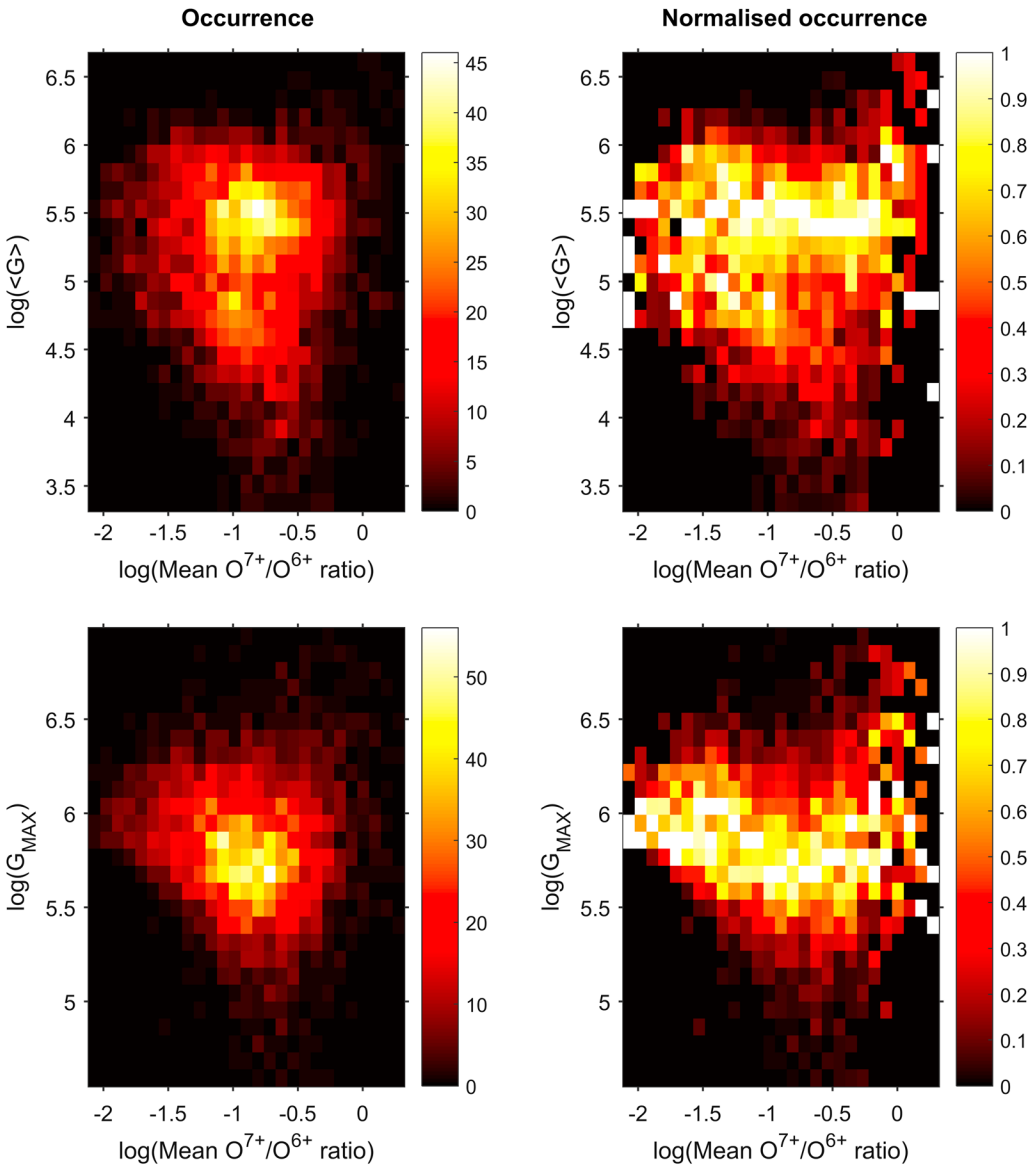

Figure 1. Histograms of the daily occurrence of solar wind O^{7+}/O^{6+} ratio and potential geoeffectiveness, *G*, using the entire ACE data set over the period 1998–2017. The top panels show $<G>$, daily means of *G*, while the bottom panels show G_{MAX}, the maximum 5-min value within a one-day window. The left panels show the raw occurrence distributions, while the right panels have been normalized, so that minimum and maximum value in each O^{7+}/O^{6+}bin is 0 and 1, respectively. Note that both axes are on a logarithmic (base 10) scale.

3. Results

In order to give an overview of the data used in this study, Figure 1 shows the relation between charge state and potential geoeffectiveness for all solar wind data from the 1998–2017 period. The data have been divided into daily intervals, for which both the mean potential geoeffectiveness ($<G>$, top panels) and the 5-min peak value (G_{MAX}, bottom panels) are calculated. The left-hand panels show occurrence histograms for the whole data set. They are dominated by the O^{7+}/O^{6} occurrence peak around 10^{-1} to $10^{-0.5}$, that is, $O^{7+}/O^{6} \approx 0.1$–0.3, typical values for the slow wind (Zhao et al., 2009). In order to highlight trends within these data, the right-hand panels show distributions normalized within each O^{7+}/O^{6+} bin, to remove the occurrence bias. The $<G>$ plot remains scattered, but for G_{MAX}, there is a general decrease with O^{7+}/O^{6+}, with a break point around 0.1, approximately the fast/slow wind transition (Crooker & McPherron, 2012; Zhao et al., 2009). This is a simple result of slow solar wind being on average less geoffective than the fast wind

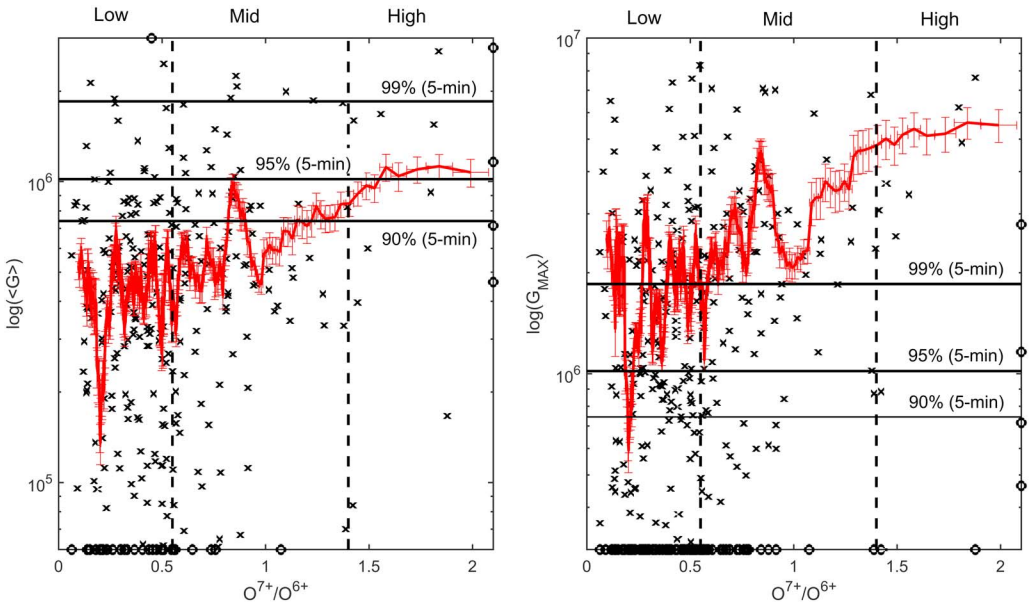

Figure 2. Potential geoeffectiveness of ICMEs as a function of their charge state. The black crosses show individual ICMEs, with the black circles indicating values outside the plotted range (discussed further in the main text). The red line shows data binned by O^{7+}/O^{6+}. Each bin contains 15 ICMEs. Bins are "rolling"; thus, each adjacent bin has 14 ICMEs in common, effectively smoothing the data. The error bars show one standard error on the mean. Left: Average *G* over the duration of an ICME. Right: Maximum 5-min value over the duration of an ICME. The solid horizontal lines show the 90, 95, and 99 percentiles over the whole 5-min *G* distribution. The dashed vertical lines show the boundaries used to define low-, middle-, and high-O^{7+}/O^{6+} ICMEs.

due to the $v^{1.83}$ dependence of *G*. It is also clear that the spread in G_{MAX} increases with O^{7+}/O^{6+}, in agreement with slow wind showing greater variability, particularly in *B* and n_P, than fast wind. ICMEs typically involve average O^{7+}/O^{6+} ratios between 0.3 and 1.5 (see Figure 2), giving log (O^{7+}/O^{6+}) in the range −0.5 to 0.2, meaning they somewhat overlap with the "hottest" part of the slow solar wind at the right-hand side of the plots in Figure 1. These highest O^{7+}/O^{6+} values show the greatest spread in *G*, as here there is a mix of ICME material, which is geoeffective, as will be demonstrated below, and the slowest solar wind, which is rarely geoeffective. Similar trends are found for iron (Fe) charge states, as they are also elevated in slow wind compared to fast wind.

While these solar wind relationships are significant, they do not order the data in a sufficient manner to be useful for space-weather forecasting. ICMEs, however, are outliers to the steady state solar wind, in terms of both their geoeffectiveness (Richardson et al., 2002) and their charge state properties (Henke et al., 1998; Lepri et al., 2001; Lepri & Zurbuchen, 2004). For most of the solar cycle, ICMEs constitute only a small fraction of the total solar wind observed in near-Earth space, though at the peak of solar maximum, the ICME contribution has been estimated to reach approximately 50% (Cane & Richardson, 2003; Riley et al., 2006). Despite ICMEs being minor constituents to the near-Earth solar wind by occurrence, they are almost exclusively responsible for severe geomagnetic storms (Richardson et al., 2002). Thus, we now consider ICMEs independent of the bulk solar wind.

In order to isolate periods of ICMEs from the steady state solar wind, we use the updated Cane and Richardson (2003) ICME catalogue, available from http://www.srl.caltech.edu/ACE/ASC/DATA/level3/icmetable2.htm. Charge state properties are averaged over the entire ICME duration. While significant variations in charge state properties are observed within individual ICMEs in near-Earth space (Akmal et al., 2001; Lepri et al., 2012; Song et al., 2016), gross charge state properties are most amenable to remote observation in the corona (Ciaravella et al., 2000; Hannah & Kontar, 2013; Lee et al., 2009), which would be necessary for any forecast scheme (discussed further in section 4). Periods classified as ICME sheath regions are included in the estimate of the associated *G*, but not in computing the average charge state of the ICME; sheath regions are compressed solar wind and so their compositional and charge state signatures will be that of the ambient

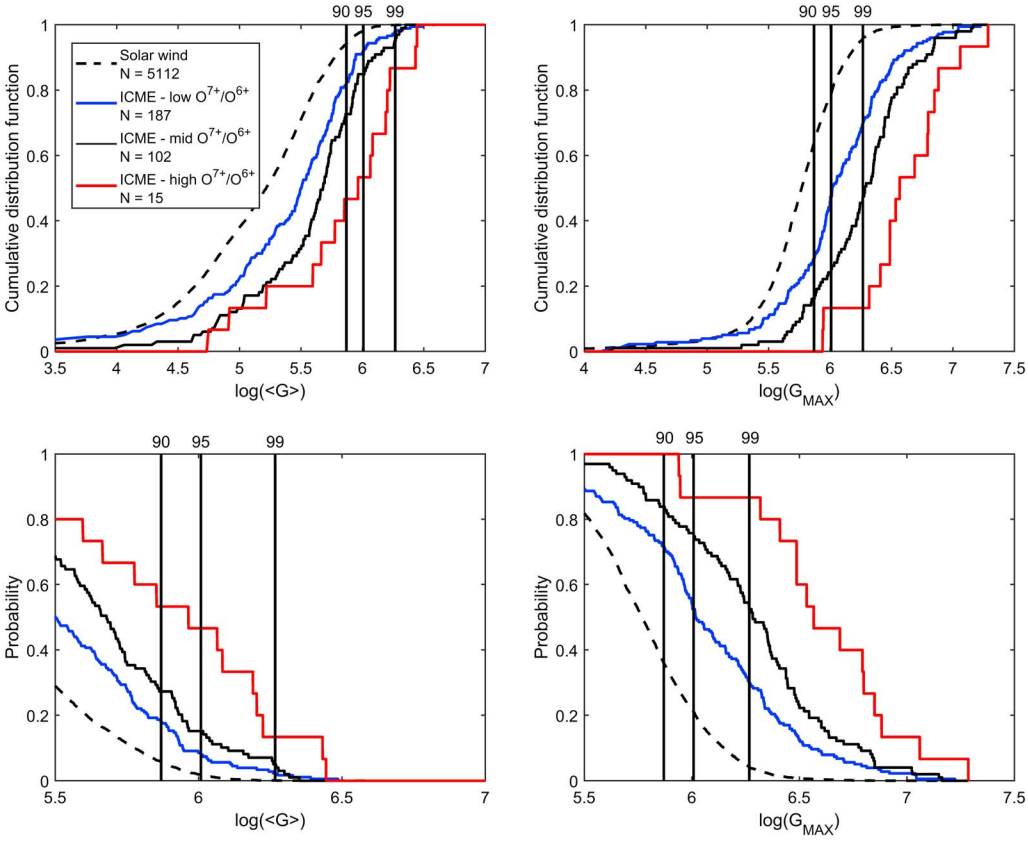

Figure 3. The statistical properties of potential geoeffectiveness, *G*, for different solar wind populations. Left and right panels consider $<G>$ and G_{MAX}, respectively. The top panels show cumulative distribution functions (CDFs) for non-ICME solar wind days (black dashed curve) and for ICMEs with low-/middle-/high-O^{7+}/O^{6+} charge state ratios (blue/black/red lines), as defined in the text. The bottom panels show probability of exceeding a given *G* threshold (i.e., 1-CDF or the "survival function"). The black vertical lines show the 90, 95, and 99 percentiles of the total 5-min *G* distribution.

solar wind, but their geoeffectiveness, particularly magnetic field intensity, is primarily a result of the speed of the driving ICME (Owens et al., 2005).

Adequate charge state and potential geoeffectiveness data are available for 304 of the catalogued ICMEs, which form the data set used in the remainder of the study. Figure 2 shows how mean *G* ($<G>$; left panels) and 5-min maximum *G* (G_{MAX}; right panels) in ICMEs vary with charge state. The circles indicate outliers, with the highest O^{7+}/O^{6+} value being 3.7, the highest/lowest $<G>$ values being $3 \times 10^6/6 \times 10^2$, and the lowest G_{MAX} value being 5×10^3. The linear correlation coefficient between $<G>$ (G_{MAX}) and O^{7+}/O^{6+} in ICMEs is 0.25 (0.32), which is relatively low, but for $N = 304$, the null hypothesis of no correlation can be rejected at the 99% confidence level. It can also be seen that simple correlation does not tell the whole story: There is a much greater range of *G* values at low O^{7+}/O^{6+} than at high O^{7+}/O^{6+}, with low *G* values largely excluded at high O^{7+}/O^{6+}. To illustrate this, the red line shows O^{7+}/O^{6+} bins defined to contain 15 ICMEs (i.e., approximately 5% of the data). Bins are "rolling," such that adjacent bins contain 14 common ICMEs, essentially smoothing the data with bins containing a constant number of points (rather than a constant parameter range). The density of points and the size of the horizontal error bars show that O^{7+}/O^{6+} bins necessarily cover a larger range at larger values (i.e., there are a great many more "cold" ICMEs with low O^{7+}/O^{6+} than there are "hot" ICMEs with high O^{7+}/O^{6+}). As quantified by the correlation coefficients, there is a good deal of scatter, but there is a clear upward trend in binned data for both measures of *G* with O^{7+}/O^{6+}. The spike in *G* around an O^{7+}/O^{6+} value of 0.7 does not seem to be the result of a single outlying point. In order to demonstrate how this relation could be used in a forecasting scenario, the ICMEs are grouped into three, somewhat arbitrary, classifications: low, middle, and high O^{7+}/O^{6+}, using thresholds of 0.55 and 1.4, shown

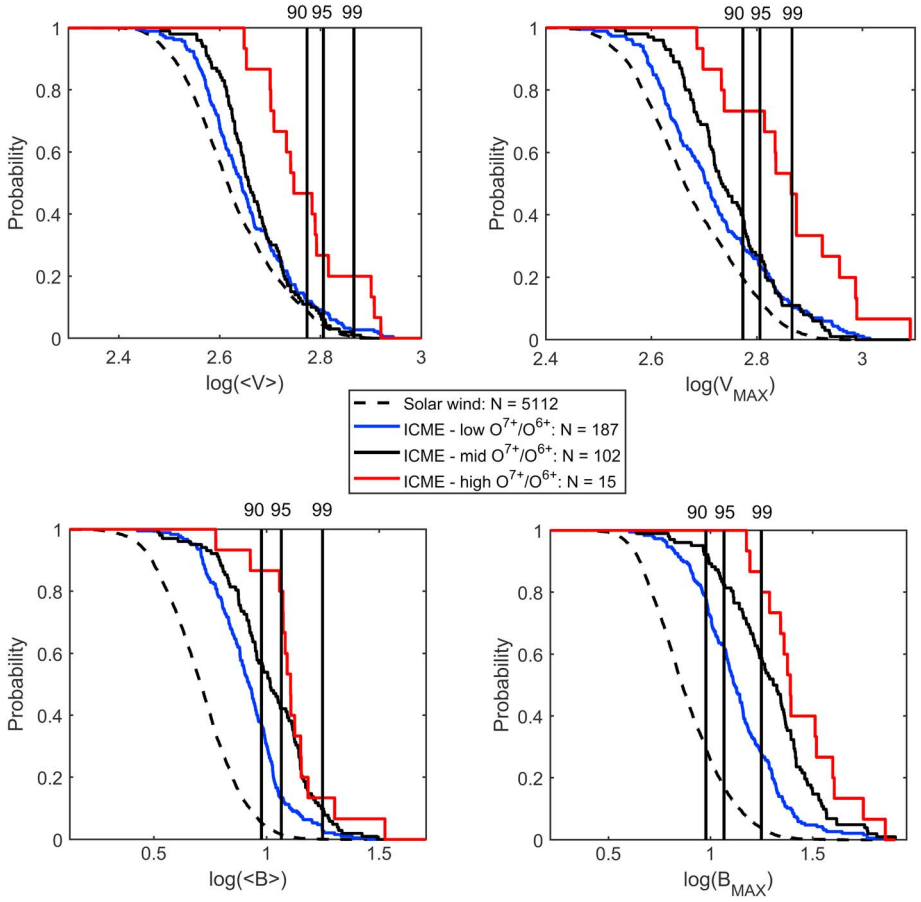

Figure 4. Probability of exceeding a given (top) speed, *V*, or (bottom) magnetic field intensity, *B*, threshold for ICMEs with low-/middle-/high-O^{7+}/O^{6+} charge state ratios (blue/black/red lines). The black vertical lines show the 90, 95, and 99 percentiles of the total 5-min *V* and *B* distributions. High-O^{7+}/O^{6+} ICMEs show significantly elevated speed and magnetic field intensities.

as the vertical dashed lines. This results in 187/102/15 low-/middle-/high-O^{7+}/O^{6+} ICMEs. In practice, these thresholds would be set by the forecast application and the severity of geomagnetic activity that is of concern. These thresholds have been purposely chosen not to contain equal number of events as forecasting, for example, the top 5% of geomagnetic activity is far more critical than forecasting the top 33%. As will be seen below, there is a monotonic increase in *G* for low-/middle-/high-O^{7+}/O^{6+} ICMEs, showing that the results presented are qualitatively robust to reasonable choice of thresholds.

Figure 3 shows the cumulative distribution functions (top) and the associated probabilities (bottom), sometimes called "survival functions," of potential geoeffectiveness in different solar wind populations. The black dashed lines show one-day intervals of the ambient solar wind with ICMEs excluded. The blue/black/red solid lines show low-/middle-/high-O^{7+}/O^{6+} ICMEs. The vertical dashed lines show the 90-, 95-, and 99-precentile values of *G* from the whole 5-min ACE data set over the period 1998–2017. The shifting of the curves to the right with increasing O^{7+}/O^{6+} shows an increased tendency for higher G values in ICMEs with hotter coronal material. For example, the probability of G_{MAX} exceeding the 99th percentile of the 5-min *G* distribution is approximately 5% for the non-ICME solar wind, 30% for low-O^{7+}/O^{6+} ICMEs, 50% for mid-O^{7+}/O^{6+} ICMEs, and 85% for high-O^{7+}/O^{6+} ICMEs. That is, there is almost a factor 3 increase in the probability of high *G* from low- to high-O^{7+}/O^{6+} ICMEs. Similarly, considering the $<G>$ distributions, an ICME having low or high O^{7+}/O^{6+} changes the probability of exceeding the 95th percentile of $<G>$ from 7% to 50%, more than a factor 7 increase.

4. Discussion and Conclusions

The geoeffectiveness of the near-Earth solar wind is determined by, in order of importance, the combined strength and orientation of the HMF relative to the Earth's own magnetic field, the solar wind speed, and the solar wind density. (Note that although solar wind number density has limited direct effect on geoeffectiveness, enhanced density results from solar wind compression, and deflection, which can also generate strong, out-of-ecliptic HMFs. Thus, solar wind density can strongly correlate with geoeffectiveness without being the causal parameter.) The greatest enhancements in HMF and solar wind speed are strongly associated the interplanetary manifestations of coronal mass ejections (ICMEs) and their sheath regions (e.g., Gosling, 1993; Richardson et al., 2002; Tsurutani et al., 1988). In order to make more "actionable" space-weather predictions (i.e., more than 1-hr lead time), forecasts must be made early in the ICME lifetime, which means while the structure is still close to the Sun. This presents difficulties both in terms of making the necessary remote observations and in terms of projecting those observations to near-Earth space.

Using white light coronagraphs and heliospheric imagers, it is possible to estimate speed and density of CMEs in the corona and inner heliosphere (e.g., Mishra et al., 2014; Yashiro et al., 2004), though they are subject to viewing and line-of-sight integration and viewing angle issues (Barnard et al., 2017). Remotely sensing the magnetic field properties of CMEs close to the Sun remains extremely difficult, though recent observational advances potentially enable the approximate orientation and sense of rotation of the CME magnetic field to be estimated (DeForest et al., 2017). There may also be empirical "rules," which can be exploited in order to place limits on the magnetic field direction within CMEs (Palmerio et al., 2017; Savani et al., 2015). Nevertheless, even taking an optimistic outlook that future observational and theoretical developments will result in routine determination of the near-Sun CME magnetic fields, these properties (as with estimates of CME speed and density) are subject to in-transit effects, such as compression, distortion, and rotation, and thus are not simple to project to near-Earth space.

As discussed in section 1, ion charge state ratios within ICMEs (and the solar wind in general) are frozen in once the electron collision rate with ions, and hence possibility of recombination, becomes negligible (Feldman et al., 2005; Geiss et al., 1995; Gloeckler et al., 2003). This is typically around a few solar radii for most ion species and coronal properties, though precise determination is sensitive to the assumed electron distribution profile (Esser & Edgar, 2000). Coronal spectroscopy enables electron temperatures to be measured within near-Sun CMEs (Ciaravella et al., 2000; Hannah & Kontar, 2013; Lee et al., 2009), and hence permits an estimate of the associated elemental charge states, which will remain unchanged to near-Earth space, regardless of in-transit processes. This study has highlighted that charge state ratios within ICMEs, particularly O^{7+}/O^{6+}, act as a useful proxy of potential geoeffectiveness, at least in a probabilistic sense. We find an approximately factor 7 increase in the probability of severe potential geoeffectiveness from low to high O^{7+}/O^{6+} ICMEs when considering one-day means, which drive geomagnetic storms, and an approximately factor 3 increase for severe 5-min peak values, which trigger more impulsive activity. A coronal spectroscopy-based forecast system would require an independent estimate of ICME arrival time in near-Earth space. Thus, it would run in tandem with the current state-of-the-art space-weather forecasting scheme, namely, solar wind simulations initialized with photospheric magnetic field observations (Riley et al., 2001) and with CME-like disturbances constrained by white-light coronagraphs and heliospheric imager observations (e.g., Mishra et al., 2014; Yashiro et al., 2004) used to initiate the modeling (Mays et al., 2015). Self-consistent modeling of ion charge states within coronal and heliospheric simulations (Shen et al., 2017) may also enable such forecasting schemes to be self-consistently combined.

Of course, the ion charge states within ICMEs have no direct bearing on the geoeffectiveness of the structure, but act as markers for other properties. Figure 4 shows that ICME charge states are correlated with both ICME magnetic field intensity (B) and ICME speed (V). In particular, the ICMEs with highest ion charge states display significantly elevated V; the probability of a high-O^{7+}/O^{6+} ICME exceeding the 95th percentile of solar wind speed (630 km/s) is nearly 5 times higher than a low- and mid-O^{7+}/O^{6+} ICME. Middle- and low-O^{7+}/O^{6+} ICMEs, however, show little difference in V.

There are two general ways in which these relations could arise and, more pertinently, affect the utility of coronal temperature observations for space weather forecasting. The first possibility is causal: The physical processes which act to elevate coronal electron temperatures (and hence charge states), also act to produce high accelerations of the associated CMEs, which is likely the result of intense magnetic fields and

reconnection (Lee et al., 2009). It has been proposed that this could be the result of flare heating of electrons (Lepri & Zurbuchen, 2004). The second possibility is that of sampling: For magnetic clouds, ICMEs, which are observed to contain a magnetic flux rope (Burlaga, 1988), the strongest *B* and out-out-heliographic magnetic fields are encountered close to the center of the flux rope. Thus, "glancing blows" of ICMEs are expected to be less geoeffective. This spatial sampling effect also results in the later arrival time of ICMEs in near-Earth space (Owens & Cargill, 2004). It has also been proposed that charge state and composition signatures exhibit systematic spatial variation within CMEs (Aguilar-Rodriguez et al., 2006; Akmal et al., 2001; Henke et al., 1998; Lepri et al., 2012; Song et al., 2016). Although even without significant spatial variation of charge state signatures within ICMEs, spatial sampling of ICMEs could still potentially explain the reported results. ICMEs originating at high latitudes are more likely to result in "glancing blows" in near-Earth space. Owing to the preferential occurrence of slow solar wind (high O^{7+}/O^{6+}) close to the equator and fast (low O^{7+}/O^{6+}) at higher latitudes, it might be expected that glancing blows would be, on average, associated with lower charge states. This will be further investigated in a future study. We do note, however, that *V* is expected to be relatively constant with spacecraft closest approach to the flux rope axis, suggesting that spatial sampling cannot fully explain the observed signatures. Of course, this interpretation relies on the paradigm of ICMEs as large-scale, coherent magnetic flux ropes, which may not be realistic (Owens et al., 2017). Thus, multispacecraft studies and global simulations are essential to fully understand the relation between ICME geoeffectiveness and ion charge states.

If spatial sampling of ICMEs is the explanation for the observed relation between charge states and potential geoeffectiveness, any forecast scheme may need to determine coronal temperatures localized along the Earth-Sun line, which would benefit from fully stereoscopic spectroscopy, such as from joint observations L5 and near-Earth space, or ideally, from L5 and L4. Nevertheless, coronal temperature diagnostics have the capability to provide a useful, additional source of space-weather forecasting information.

Acknowledgments
M. O., M. L., and L. B. are part-funded by Science and Technology Facilities Council (STFC) grant ST/M000885/1 and Natural Environment Research Council (NERC) grant NE/P016928/1. Solar wind composition and ion charge state information are provided by the ACE Solar Wind Ion Composition Spectrometer (SWICS) instrument (Gloeckler et al., 1998), here taken from the 3-hr "merged" data set at ftp://cdaweb.gsfc.nasa.gov/pub/data/ace/multi. ACE solar wind magnetic field and plasma data (McComas et al., 1998; Smith et al., 1998) were obtained from ftp://cdaweb.gsfc.nasa.gov.

References

Aguilar-Rodriguez, E., Blanco-Cano, X., & Gopalswamy, N. (2006). Composition and magnetic structure of interplanetary coronal mass ejections at 1 AU. *Advances in Space Research*, *38*(3), 522–527. https://doi.org/10.1016/j.asr.2005.01.051

Akmal, A., Raymond, J. C., Vourlidas, A., Thompson, B., Ciaravella, A., Ko, Y.-K., et al. (2001). SOHO observations of a coronal mass ejection. *The Astrophysical Journal*, *553*(2), 922–934. https://doi.org/10.1086/320971

Barnard, L. A., de Koning, C. A., Scott, C. J., Owens, M. J., Wilkinson, J., & Davies, J. A. (2017). Testing the current paradigm for space weather prediction with heliospheric imagers. *Space Weather*, *15*, 782–803. https://doi.org/10.1002/2017SW001609

Burlaga, L. F. (1988). Magnetic clouds: Constant alpha force-free configurations. *Journal of Geophysical Research*, *93*(A7), 7217–7224.

Cane, H. V., & Richardson, I. G. (2003). Interplanetary coronal mass ejections in the near-Earth solar wind during 1996–2002. *Journal of Geophysical Research*, *108*(A4), 1156. https://doi.org/10.1029/2002JA009817

Ciaravella, A., Raymond, J., Thompson, B., Van Ballegooijen, A., Strachan, L., Li, J., et al. (2000). Solar and heliospheric observatory observations of a helical coronal mass ejection. *The Astrophysical Journal*, *529*(1), 575–591. https://doi.org/10.1086/308260

Crooker, N. U., & McPherron, R. L. (2012). Coincidence of composition and speed boundaries of the slow solar wind. *Journal of Geophysical Research*, *117*, A09104. https://doi.org/10.1029/2012JA017837

Davis, C. J., Davies, J. A., Lockwood, M., Rouillard, A. P., Eyles, C. J., & Harrison, R. A. (2009). Stereoscopic imaging of an Earth-impacting solar coronal mass ejection: A major milestone for the STEREO mission. *Geophysical Research Letters*, *360*, L08102. https://doi.org/10.1029/2009GL038021

DeForest, C., de Koning, C., & Elliott, H. (2017). 3D polarized imaging of coronal mass ejections: Chirality of a CME. *The Astrophysical Journal*, *850*(2), 130. https://doi.org/10.3847/1538-4357/aa94ca

Dungey, J. W. (1961). Interplanetary magnetic field and the auroral zones. *Physical Review Letters*, *6*(2), 47–48. https://doi.org/10.1103/PhysRevLett.6.47

Esser, R., & Edgar, R. J. (2000). Reconciling spectroscopic electron temperature measurements in the solar corona with in situ charge state observations. *The Astrophysical Journal Letters*, *532*(1), L71–L74. https://doi.org/10.1086/312548

Feldman, U., Landi, E., & Schwadron, N. (2005). On the sources of fast and slow solar wind. *Journal of Geophysical Research*, *110*, A07109. https://doi.org/10.1029/2004JA010918

Geiss, J., Gloeckler, G., & von Steiger, R. (1995). Origin of the solar wind from composition data. *Space Science Reviews*, *72*(1-2), 49–60. https://doi.org/10.1007/BF00768753

Gloeckler, G., Cain, J., Ipavich, F., Tums, E., Bedini, P., Fisk, L., et al. (1998). Investigation of the composition of solar and interstellar matter using solar wind and pickup ion measurements with SWICS and SWIMS on the ACE spacecraft. In C. T. Russell, R. A. Mewaldt, & T. T. Von Rosenvinge (Eds.), *The advanced composition explorer mission* (pp. 497–539). Dordrecht, Netherlands: Springer. https://doi.org/10.1007/978-94-011-4762-0_18

Gloeckler, G., Zurbuchen, T. H., & Geiss, J. (2003). Implications of the observed anticorrelation between solar wind speed and coronal electron temperature. *Journal of Geophysical Research*, *108*(A4), 1158. https://doi.org/10.1029/2002JA009286

Gonzalez, W. D., Tsurutani, B. T., & Clúa de Gonzalez, A. L. (1999). Interplanetary origin of geomagnetic storms. *Space Science Reviews*, *88*(3), 529–562. https://doi.org/10.1023/A:1005160129098

Gopalswamy, N., Lara, A., Yashiro, S., Kaiser, M. L., & Howard, R. A. (2001). Predicting the 1-AU arrival times of coronal mass ejections. *Journal of Geophysical Research*, *106*(A12), 29,207–29,217. https://doi.org/10.1029/2001JA000177

Gosling, J. T. (1993). The solar flare myth. *Journal of Geophysical Research*, *98*(A11), 18,937–18,950. https://doi.org/10.1029/93JA01896

Hannah, I., & Kontar, E. (2013). Multi-thermal dynamics and energetics of a coronal mass ejection in the low solar atmosphere. *Astronomy & Astrophysics*, *553*(A10). https://doi.org/10.1051/0004-6361/201219727
Henke, T., Woch, J., Mall, U., Livi, S., Wilken, B., Schwenn, R., et al. (1998). Differences in the O7+/O6+ ratio of magnetic cloud and non-cloud coronal mass ejections. *Geophysical Research Letters*, *25*(18), 3465–3468. https://doi.org/10.1029/98GL02632
Kappenman, J. G. (2003). Storm sudden commencement events and the associated geomagnetically induced current risks to ground-based systems at low-latitude and midlatitude locations. *Space Weather*, *1*(3), 1016. https://doi.org/10.1029/2003SW000009
Kilpua, E., Koskinen, H. E. J., & Pulkkinen, T. I. (2017). Coronal mass ejections and their sheath regions in interplanetary space. *Living Reviews in Solar Physics*, *14*(1), 5. https://doi.org/10.1007/s41116-017-0009-6
Lee, J.-Y., Raymond, J., Ko, Y.-K., & Kim, K.-S. (2009). Three-dimensional structure and energy balance of a coronal mass ejection. *The Astrophysical Journal*, *692*(2), 1271–1286. https://doi.org/10.1088/0004-637X/692/2/1271
Lepri, S. T., Laming, J. M., Rakowski, C. E., & Von Steiger, R. (2012). Spatially dependent heating and ionization in an ICME observed by both ACE and Ulysses. *The Astrophysical Journal*, *760*(2), 105. https://doi.org/10.1088/0004-637X/760/2/105
Lepri, S. T., & Zurbuchen, T. H. (2004). Iron charge state distributions as an indicator of hot ICMEs: Possible sources and temporal and spatial variations during solar maximum. *Journal of Geophysical Research*, *109*, A01112. https://doi.org/10.1029/2003JA009954
Lepri, S. T., Zurbuchen, T. H., Fisk, L. A., Richardson, I. G., Cane, H. V., & Gloeckler, G. (2001). Iron charge distribution as an identifier of interplanetary coronal mass ejections. *Journal of Geophysical Research*, *106*(A12), 29,231–29,238. https://doi.org/10.1029/2001JA000014
Lockwood, M. (2013). Reconstruction and prediction of variations in the open solar magnetic flux and interplanetary conditions. *Living Reviews in Solar Physics*, *10*, 4. https://doi.org/10.12942/lrsp-2013-4
Lockwood, M., Owens, M. J., Barnard, L. A., Bentley, S., Scott, C. J., & Watt, C. E. (2016). On the origins and timescales of geoeffective IMF. *Space Weather*, *14*, 406–432. https://doi.org/10.1002/2016SW001375
Lockwood, M., Owens, M. J., Barnard, L. A., Scott, C. J., & Watt, C. E. (2017). Space climate and space weather over the past 400 years: 1. The power input to the magnetosphere. *Journal of Space Weather and Space Climate*, *7*, A25. https://doi.org/10.1051/swsc/2017019
Manchester, W., Kilpua, E. K. J., Liu, Y. D., Lugaz, N., Riley, P., Török, T., & Vršnak, B. (2017). The physical processes of CME/ICME evolution. *Space Science Reviews*, *212*(3), 1159–1219. https://doi.org/10.1007/s11214-017-0394-0
Mays, M. L., Taktakishvili, A., Pulkkinen, A., MacNeice, P. J., Rastätter, L., Odstrcil, D., et al. (2015). Ensemble modeling of CMEs using the WSA–ENLIL+Cone model. *Solar Physics*, *290*(6), 1775–1814. https://doi.org/10.1007/s11207-015-0692-1
McComas, D. J., Bame, S. J., Barker, S. J., Feldman, W. C., Phillips, J. L., Riley, P., & Griffee, J. W. (1998). Solar wind electron proton alpha monitor (SWEPAM) for the Advanced Composition Explorer. *Space Science Reviews*, *86*(1/4), 563–612. https://doi.org/10.1023/A:1005040232597
Mishra, W., Srivastava, N., & Davies, J. A. (2014). A comparison of reconstruction methods for the estimation of coronal mass ejections kinematics based on SECCHI/HI observations. *The Astrophysical Journal*, *784*(2), 135. https://doi.org/10.1088/0004-637X/784/2/135
Owens, M. J., & Cargill, P. J. (2004). Predictions of the arrival time of coronal mass ejections at 1 AU: An analysis of the causes of errors. *Annales de Geophysique*, *22*(2), 661–671.
Owens, M. J., Cargill, P. J., Pagel, C., Siscoe, G. L., & Crooker, N. U. (2005). Characteristic magnetic field and speed properties of interplanetary coronal mass ejections and their sheath regions. *Journal of Geophysical Research*, *110*, A01105. https://doi.org/10.1029/2004JA010814
Owens, M. J., Challen, R., Methven, J., Henley, E., & Jackson, D. R. (2013). A 27 day persistence model of near-Earth solar wind conditions: A long lead-time forecast and a benchmark for dynamical models. *Space Weather Journal*, *11*, 225–236. https://doi.org/10.1002/swe.20040
Owens, M. J., & Forsyth, R. J. (2013). The heliospheric magnetic field. *Living Reviews in Solar Physics*, *10*, 5. https://doi.org/10.12942/lrsp-2013-5
Owens, M. J., Lockwood, M., & Barnard, L. A. (2017). Coronal mass ejections are not coherent magnetohydrodynamic structures. *Scientific Reports*, *7*(1), 4152. https://doi.org/10.1038/s41598-017-04546-3
Palmerio, E., Kilpua, E. K. J., James, A. W., Green, L. M., Pomoell, J., Isavnin, A., & Valori, G. (2017). Determining the intrinsic CME flux rope type using remote-sensing solar disk observations. *Solar Physics*, *292*(2), 39. https://doi.org/10.1007/s11207-017-1063-x
Richardson, I. G., Cane, H. V., & Cliver, E. W. (2002). Sources of geomagnetic activity during nearly three solar cycles (1972–2000). *Journal of Geophysical Research*, *107*(A8), 1187. https://doi.org/10.1029/2001JA000504
Riley, P., Ben Nun, M., Linker, J., Owens, M. J., & Horbury, T. S. (2017). Forecasting the properties of the solar wind using simple pattern recognition. *Space Weather*, *15*, 526–540. https://doi.org/10.1002/2016SW001589
Riley, P., Linker, J. A., & Mikic, Z. (2001). An empirically-driven global MHD model of the solar corona and inner heliosphere. *Journal of Geophysical Research*, *106*(A8), 15,889–15,902.
Riley, P., Schatzman, C., Cane, H. V., Richardson, I. G., & Gopalswamy, N. (2006). On the rates of coronal mass ejections: Remote solar and in situ observations. *The Astrophysical Journal*, *647*(1), 648–653. https://doi.org/10.1086/505383
Rosenberg, R. L., & Coleman, P. J. (1969). Heliographic latitude dependence of the dominant polarity of the interplanetary magnetic field. *Journal of Geophysical Research*, *74*(24), 5611–5622. https://doi.org/10.1029/JA074i024p05611
Russell, C., and, and R. McPherron (1973), Semiannual variation of geomagnetic activity, *Journal of Geophysical Research*, *78*(1), 92–108. https://doi.org/10.1029/JA078i001p00092
Savani, N. P., Owens, M. J., Rouillard, A. P., Forsyth, R. J., & Davies, J. A. (2010). Observational evidence of a coronal mass ejection distortion directly attributable to a structured solar wind. *The Astrophysical Journal. Letters*, *714*(1), L128–L132. https://doi.org/10.1088/2041-8205/714/1/L128
Savani, N. P., Vourlidas, A., Szabo, A., Mays, M. L., Richardson, I. G., Thompson, B. J., et al. (2015). Predicting the magnetic vectors within coronal mass ejections arriving at Earth: 1. Initial architecture. *Space Weather*, *13*, 374–385. https://doi.org/10.1002/2015SW001171
Schwenn, R. (2006). Space weather: The solar perspective. *Living Reviews in Solar Physics*, *3*, 2. https://doi.org/10.12942/lrsp-2006-2
Shen, C., Raymond, J. C., Mikić, Z., Linker, J. A., Reeves, K. K., & Murphy, N. A. (2017). Time-dependent ionization in a steady flow in an MHD model of the solar corona and wind. *The Astrophysical Journal*, *850*(1), 26. https://doi.org/10.3847/1538-4357/aa93f3
Siscoe, G., & Crooker, N. (1996). Diurnal oscillation of Dst: A manifestation of the Russell-McPherron effect. *Journal of Geophysical Research*, *101*(A11), 24,985–24,989. https://doi.org/10.1029/96JA01875
Smith, C. W., L'Heureux, J., Ness, N. F., Acuna, M. H., Burlaga, L. F., & Scheifele, J. (1998). The ACE magnetic fields experiment. *Space Science Reviews*, *86*(1/4), 613–632. https://doi.org/10.1023/A:100509221
Song, H., Zhong, Z., Chen, Y., Zhang, J., Cheng, X., Zhao, L., et al. (2016). A statistical study of the average iron charge state distributions inside magnetic clouds for solar cycle 23. *The Astrophysical Journal Supplement Series*, *224*(2), 27. https://doi.org/10.3847/0067-0049/224/2/27
Tsurutani, B. T., Gonzalez, W. D., Tang, F., Akasofu, S. I., & Smith, E. J. (1988). Origin of the interplanetary southward magnetic fields responsible for the major magnetic storms near solar maximum (1978–1979). *Journal of Geophysical Research*, *93*(A8), 8519.
Tucker-Hood, K., Scott, C., Owens, M., Jackson, D., Barnard, L., Davies, J. A., et al. (2015). Validation of a priori CME arrival predictions made using real-time heliospheric imager observations. *Space Weather*, *13*, 35–48. https://doi.org/10.1002/2014SW001106

Vasyliunas, V. M., Kan, J. R., Siscoe, G. L., & Akasofu, S.-I. (1982). Scaling relations governing magnetospheric energy transfer. *Planetary and Space Science*, *30*(4), 359–365. https://doi.org/10.1016/0032-0633(82)90041-1

Yashiro, S., Gopalswamy, N., Michalek, G., St Cyr, O. C., Plunkett, S. P., Rich, N. B., & Howard, R. A. (2004). A catalog of white light coronal mass ejections observed by the SOHO spacecraft. *Journal of Geophysical Research*, *109*, A07105. https://doi.org/10.1029/2003JA010282

Zhao, L., Zurbuchen, T. H., & Fisk, L. A. (2009). Global distribution of the solar wind during solar cycle 23: ACE observations. *Geophysical Research Letters*, *36*, L14104. https://doi.org/10.1029/2009GL039181